Development of a novel testing methodology for in-situ microstructural

characterisation during continuous strain path change

Sisir Dhara[a,*], Scott Taylor[a], Łukasz Figiel[a], Darren Hughes[a], Sumit Hazra[a]

[a] WMG, University of Warwick, Coventry, CV4 7AL, UK

* Corresponding author's mail id: Sisir.Dhara@warwick.ac.uk

Abstract

Strain path transition is a common phenomenon during continuous stamping operations of sheet metal and can potentially alter the forming limit of the material. Enabling strain path change in a single experiment is a key challenge faced by several researchers. To understand the effect of continuous strain path change on material forming limits, detailed material characterisation is needed where the material is deformed while the strain path of the material is changed continuously. In this work, a test method was developed, which consisted of a novel mechanical rig and specimen design. The mechanism allowed DP600 steel and AA5182-O aluminium samples to change strain paths continuously without unloading the specimen. Digital image correlation measurements of the strain evolution of the samples during tests showed that the technique was able to alter the strain path of the sample from uniaxial to biaxial strain path. In particular, the measurements showed that the transition from uniaxial to biaxial strain paths was sharper in DP600 than AA5182-O. The test was repeated in a scanning electron microscope (SEM) chamber to observe the behaviour of the microstructure during the strain path transition. The microstructural strain evolution showed rotation of strain bands while the evolution of electron back scattered diffraction (EBSD) maps conveyed grain rotation during continuous strain path change in both the materials. The

23 strain path transition controlled the rotation of grains with preferred crystallographic

24 orientations.

25 **Keywords:** Sheet Metal Stamping, Strain Path Change, Finite Element Modelling,

26 Microstructure Characterisation, In-situ SEM, In-situ EBSD.

1   Introduction

28   Stamping processes used in the automotive industry are often multi-stage. In the first

29 stage, the material undergoes the majority of its final deformation as the sheet is drawn. In

30 subsequent stages, the drawn material may be redrawn, flanged or pierced to produce the

31 final panel geometry. This process results in two types of strain path change mechanisms:

32 continuous and discontinuous. The continuous strain path change takes place during the draw

33 stage when the material flows over the changing geometry of the draw tool, which alters the

34 strain path of the material as it is deformed from one location to the next. The discontinuous

35 strain path change mechanism occurs when the component is removed from the draw tooling

36 and allowed to springback. It is subsequently deformed along a different strain path when it is

37 re-drawn or flanged in a following stage.

38   The current state-of-the-art has focussed on the effects of the discontinuous strain path

39 change on material forming limit. Dhara et al. [1] simulated the discontinuous strain path

40 change in an AA5754-O aluminium alloy by first pre-strained in uniaxially in a tensile

41 machine and subsequently re-loading along the biaxial strain path using a miniature Nakajima

42 test. They found considerable increase in the forming limits when the material was pre-

43 strained along transverse to the sheet rolling direction. More recently, Collins et al. [2]

44 observed a similar phenomenon in low carbon ferritic steel samples. Using a purpose-built

45 tester, cruciform samples were first pre-strained along a uniaxial strain path, afterwards

46 unloaded and then loaded biaxially. They found a significant increase in the limit strains.

47   The effect of the continuous strain path change on forming limits has not been studied as

48   thoroughly. Song et al. [3] and Leotoing and Guines [4] developed a complex cruciform

49   specimen to change the strain path continuously from uniaxial tension to biaxial tension using

50   a sophisticated servo-hydraulic testing machine. They found that continuously changing

51   strain paths also produced significant changes to the forming limit strains in steel (DP600)

52   and aluminium (AA5086). However, the study of continuous strain path change mechanism

53   with a simple specimen geometry and a simpler biaxial stretching mechanism is potentially

54   more important to understand the reason behind the formability change during the strain path

55   change that occurs in the draw stage.

56   One potential route to address the effect of continuous strain path changes is to

57   characterise forming limits in the stress space. Stoughton [5] and Stoughton and Zhu [6]

58   concluded that the stress based forming limit curve seemed to be an attractive tool to predict

59   the formability of sheet metal subjected to strain path change during the multi-stage

60   deformation process. Yoshida et al [7] and Yoshida and Kuwabara [8] studied forming limit

61   stresses and strains of a steel alloy by deforming tube samples through linear and combined

62   linear stress paths. They made three findings. First, the stress-based characterisation of

63   forming limits was path independent when the strain path change was discontinuous. Second,

64   the limit stress was path *dependent* when it was *continuous*. Third, path-dependent nature was

65   directly affected by the strain hardening behaviour of the material. Hence, it is necessary to

66   evaluate the stress and strain evolution as well as the strain hardening behaviour of a material

67   during continuous strain path change to understand the effect of continuous strain path

68   change on formability.

69   To identify the relationship between strain path change and microstructure, Verma et

70   al. [9] studied the strain hardening behaviour and evolution of yield surface of ultra-low

71   carbon high strength automotive steel during discontinuous strain path changes. They found

72 that as material strain hardened, its dislocation density increased; and the initial crystal

73 structure of the material became distorted and re-oriented. Correspondingly, its yield surface

74 changed size and shape as well as in its positioning in the stress space. Similarly, Erinosho et

75 al. [10,11] investigated the relationship among strain hardening behaviour, dislocation

76 density and crystal structure of steel during discontinuous strain path change. They concluded

77 that the orientation of grains in the crystal structure or the texture of the material were

78 important factors in the strain hardening behaviour and evolution of the dislocation density of

79 the material during the discontinuous strain path change. Furthermore, the texture and

80 dislocation density evolution affected the strain localisation and eventually the limit strain of

81 the material. However, strain hardening and texture evolution during continuous strain path

82 change has not been reported.

83   The current material models to describe the strain hardening behaviour of a material

84 were developed for discontinuous strain path change in microscopic level [12–14] and in

85 macroscopic level [15–17] by considering the dataset from discontinuous strain path change

86 experiments. The experimental limitation to study continuous strain path change hindered the

87 investigation of the strain hardening behaviour, evolution of yield surface and evolution of

88 crystal structure of a material. Hence, study of continuous train path change is extremely

89 important to understand its effect on the strain hardening behaviour, evolution of yield

90 surface and evolution of crystal structure of a material to understand the path dependent

91 behaviour of forming limit strains and stresses effectively.

92   To investigate the relationship between applied deformation and microstructures, in-

93 situ deformation techniques are frequently used. During in-situ deformation, a material is

94 elongated using a micromechanical test rig that is placed in a scanning electron microscope

95 (SEM) chamber to characterise microstructural evolution during deformation. This may be

96 done using detectors such as the secondary electron or electron back-scatter diffraction

97 (EBSD) to image and measure texture respectively. Ghadbeigi et al. [18] and Celotto et al.

98 [19] deformed dual-phase 1000 (DP1000) steel and transformation induced plasticity 800

99 (TRIP800) steel samples uniaxially using a miniaturised loading rig. They captured SEM

100 images of the sample surface and post-processed the images using the digital image

101 correlation (DIC) technique to analyse the evolution of strain distribution in the ferritic and

102 martensitic phases of their specimens. Caër and Pesci [20] used a Micromecha

103 micromechanical test rig to biaxially stretch cruciform samples of annealed AISI 304

104 stainless steel to measure the evolution of texture from the centre of the biaxial specimen

105 during the loading process. They analysed the data to understand the grain rotation and

106 misorientation development in the material and found that the loading path had the potential

107 to orient the grains along a specific crystallographic direction.

108   A common characteristic of these in-situ experiments was that the specimen was

109 restricted to single strain path deformation. As a result, the effect of continuous strain path

110 changes on microstructure and texture has not been studied, and as such there is a research

111 gap in the understanding of material behaviour during this type of deformation. Addressing

112 this gap will enable formability to be quantified more accurately, thereby increasing the

113 confidence for designers in utilising high strength materials that have low formability.

114   This work developed an experimental method to enable continuous strain path change in

115 a sample that can be carried out in an SEM chamber to relate applied loading to

116 microstructural evolution. The design of rig and sample was developed with the help of

117 finite-element models and subsequent physical tests showed that the design was able to

118 continuously change strain path of a sample. Tests were carried out on steel and aluminium

119 specimens. Their behaviour was observed with digital image correlation (to measure strain at

120 two length scales namely macroscale and microscale) and EBSD. The strain results at

121 macroscale (termed as macro-strain) showed that aluminium displayed a 'lag' in transitioning

122 to the second strain path that was not observed in steel. The strain at microscale (termed as

123 micro-strain) showed rotation of strain banding over the microstructure of the samples. The

124 EBSD results indicated the observable microstructural and textural changes prominently in

125 grain rotation.

2 Development of a novel continuous strain path change mechanism

127   A Micromecha Proxima test rig was used to perform the strain path change experiment.

128 The cruciform sample design proposed by Caër and Pesci [20] was modified to allow a strain

129 path change from uniaxial to biaxial when used with the Micromecha rig. The modification

130 and optimisation of the sample design was carried out by creating an FE model of the

131 experiment particularly, ensuring that the strain path transition occurs after a prescribed

132 amount of pre-strain. The sample design was then validated by carrying out experiments on

133 steel and aluminium samples. Three repetitions were performed for each set of experiments.

2.1   Optimisation of specimen design

135   The experimental set-up of the Micromecha Proxima rig fitted with the cruciform

136 sample is presented in Figure 1. The 'inline' grips and 'transverse' grips of the rig are

137 connected through a 45° wedge (Figure 1a). A motor pulls the inline grip 1 against inline grip

138 2, which is securely grounded to the body of the rig. As the motor moves the inline grip 1

139 along $+x$ direction, its motion is translated into a perpendicular motion of the transverse grips

140 (in the $+y$ and $-y$ direction) via the wedge connection. To change the strain path during the

141 experiment, the specimen geometry was modified to include slotted holes in the vertical arms

142 (Figure 2a). The overall dimension of the strain path change sample was 30.4 mm by 30 mm

143 (Figure 2a). The central region was reduced in thickness to concentrate the strain

144 accumulation and to prevent overloading the rig and the load cell.

145   At the start of the experiment, the slots allowed the connecting bolts of the transverse

146   grips (Figure 1a) to translate without loading the specimen. After a specified elongation that

147   was determined by the length of the slots (0.2 mm) (Figure 2b), the connecting bolts of the

148   transverse grips engaged the specimen and the specimen was deformed biaxially. Hence, the

149   material was deformed uniaxially at the start of the experiment and thereafter the strain path

150   of the material was changed to biaxial strain path, without unloading the sample. Before

151   starting the test, the tolerance on the sample holes and slots and the design of the rig ensured

152   that the sample was located symmetrically. Specifically, while placing the specimen in the

153   rig, it was ensured that the arms with standard hole (not the slots) were placed parallel to the

154   x-axis and gripped with serrated clamps. The clamps and the slot restricted any rotation about

155   the centre of the sample during uniaxial deformation. During the transition, the slots ensured

156   that the sample was able to deform parallel to the y-axis. The slot length was chosen a value

157   of 0.2 mm to allow a reasonable amount of deformation along the uniaxial strain path before

158   the strain path transitioned to biaxial strain path. This value may be changed to allow

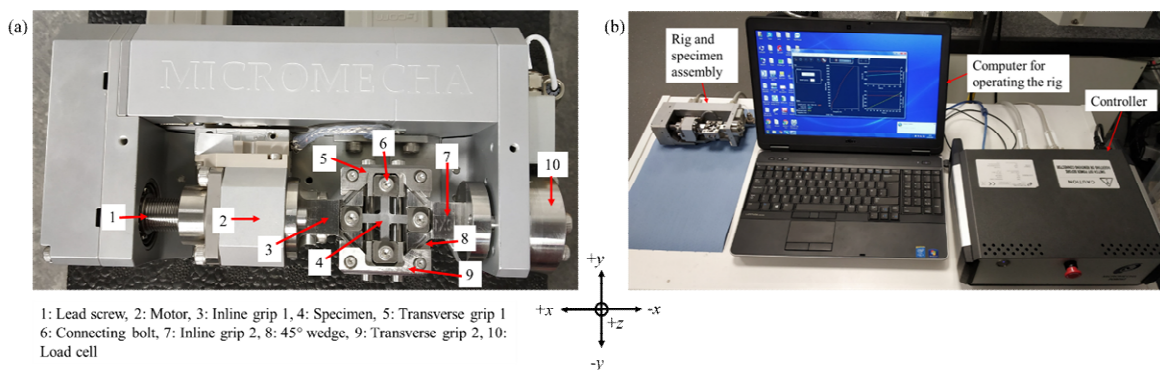159   different levels of deformation along the uniaxial strain path.

160

161   Figure 1: Experimental set-up consisting of (a) the Micromecha Proxima rig and the

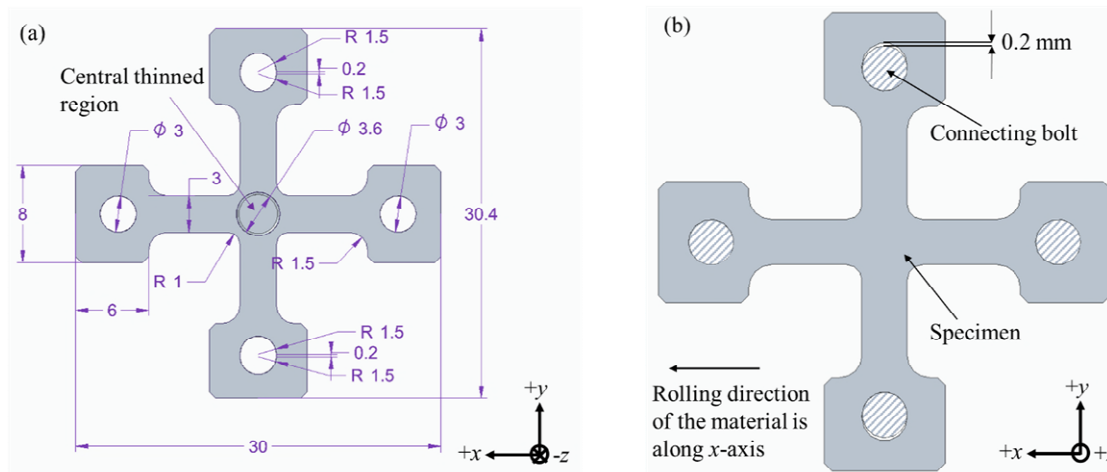162   specimen; and (b) all other accessories.

163

164   Figure 2: Design of (a) strain path change specimen and (b) assembly showing 0.2 mm travel

165   of connecting bolt during strain path change.

2.2   Choice of specimen materials

167   AA5182-O aluminium alloy and DP600 steel were chosen as specimen materials

168   because they are commonly used in automotive applications. AA5182-O is a single-phase

169   material and DP600 is a dual-phase material made up of a hard martensite phase and a softer

170   ferrite phase. The material properties and chemical compositions are detailed in Table 1 [21–

171   28] and Table 2 [21,22,27,29] respectively. The as-received thickness of aluminium and steel

172   sheets were 1 mm and 1.2 mm respectively. The thickness of central thinned region was 0.3

173   mm for aluminium and 0.25 mm for steel specimens. The higher thickness at the central

174   region in aluminium sample was chosen as the same sample was utilised for microscopic

175   observation after polishing and the material removal during polishing was higher for

176   aluminium than steel. In this work, the length of the slots was kept same for both the

177   aluminium and steel samples.

178   Table 1: Material properties of AA5182-O aluminium alloy and DP600 steel used in this

179   work [21–28]

Material		AA5182-O	DP600
Gauge (mm)		1	1.2
Thickness of central thinned region (mm)		0.3	0.25
Young modulus (GPa)		70	208
Yield strength (MPa)		130	407
Ultimate tensile strength (MPa)		282	665
% Elongation		20	22
Anisotropy parameters	r_0	0.75	0.96
	r_{45}	0.85	0.93
	r_{90}	0.85	1.05
Hardening parameters according to Hollomon law	Strength coefficient, K (MPa)	487.6	1125
	Hardening exponent, n	0.263	0.21
Density (g/cm^3)		2.6	7.87
Poisson's ratio		0.33	0.3

180

181   Table 2: Chemical composition (wt %) of AA5182-O and DP600 material used in this work

182   [21,22,27,29]

Material	Mg	Mn	Fe	Si	Al
AA5182-O	4.3	0.34	0.21	0.03	Balance

Material	C	Mn	Si	Al	Mo	Cr	Cu	S	P	Fe
DP600	0.09	1.84	0.36	0.05	0.01	0.02	0.03	0.005	0.01	Balance

183

184 **2.3 FE modelling of continuous strain path transition**

185   The grips, connecting bolts and the specimen were modelled using the finite element

186 (FE) method to optimise the experiment and the sample design (Figure 3). The horizontal

187 grips, vertical grips, connecting bolts (Figure 3) were modelled as rigid bodies and the

188 specimen of which the gripping areas were modelled as rigid bodies while the rest of the part

189 of the specimen (indicated by red colour in Figure 3) was modelled as a deformable body. All

190 bodies in the entire model were meshed with solid elements of an appropriate size that

191 optimised speed and accuracy. The sample was assumed to yield isotropically (using the von

192 Mises model) and power-law hardening was assumed. The material properties used in the

193 modelling are tabulated in Table 1. To model the joint between the specimen to the grips, the

194 nodes in the connecting bolts and the nodes of the grips were modelled as constrained rigid

195 bodies while the connecting bolts were making surface contact with the griping areas of the

196 specimen. Two boundary conditions were applied to the model. First, displacement (2.5 mm

197 for AA5182-O and 1.5 mm for DP600) was applied to in-line grip 1 along x-axis (Figure 3) to

198 represent the motor in the physical rig. Inline grip 2 was fixed. Second, the motion of

199 transverse grips 1 and 2 was restricted to the y-axis, to reflect the physical rig. The model was

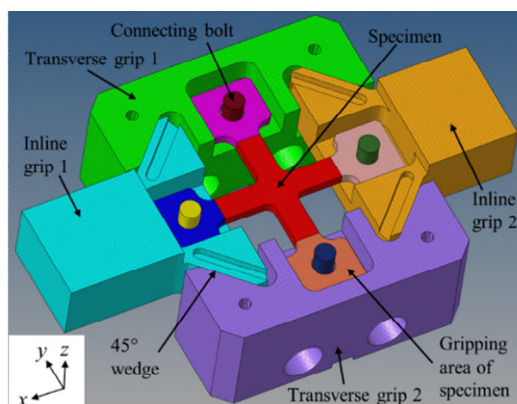200 solved using LS-Dyna explicit v.10.1.0.

201

202 Figure 3: FE model of the assembly consists of the grips, connecting bolts and the specimen

203 **2.4   Experimental validation of strain path change model**

204   The developed FE model for strain path change was validated against experimental trials

205   of AA5182-O and DP600 specimens. The specimens were machined in a high precision CNC

206   milling machine (DATRON M7HP machine) with a dimensional tolerance of the holes and

207   slots of 0.005 mm. The design of the sample ensured that the inline grips elongated the

208   sample uniaxially along *x*-axis up to 0.2 mm before the transverse grips applied loading on

209   the sample along *y*-axis to deform the sample biaxially. The macro-strain evolution over the

210   entire surface area (30 mm X 30 mm approx.) of the sample was measured with a GOM 12 M

211   DIC system. The DIC system consisted of two 12MP cameras fitted with 75 mm lenses to

212   capture the images of the arms and central region of the specimens. A speckled paint pattern

213   was applied to the sample surface before the test and GOM ARAMIS version 6.1 software

214   was used to acquire and process the captured images to calculate strain contour [30,31]. The

215   images were captured at 1 frame/second and the rig stretched the samples at a rate of 0.3

216   mm/min along *x*-axis (Figure 3).

217 **3   Measuring of micro-strain and texture evolution during continuous**

218   **strain path change**

219   Following the validation of the design of the continuous strain path change specimen, the

220   tests were repeated in a Zeiss Sigma SEM to demonstrate the capability of measuring the

221   micro-strain and texture evolution at the central thinned region of the sample. Particular

222   attention was placed on the capability of observing the behaviour of the micro-strain and

223   textural evolution during the strain path transition.

224   Prior to the experiments, the AA5182-O and DP600 specimens were prepared by

225   standard mechanical polishing to a final physical stage using colloidal silica. To measure the

11

226 micro-strain evolution, samples were additionally etched to highlight the features in the

227 microstructure. AA5182-O samples were etched with 10% NaOH aqueous solution for 2

228 minutes while DP600 samples were etched with 2% Nital solution for 10 seconds. These

229 microstructural features were used as the pattern in this study from which the micro-strain

230 was evaluated by correlating the micrographs between two successive deformation steps

231 using DIC analysis [18].

232   Loading of samples was controlled by Micromecha's POROS 2 software. Load and

233 extension were captured by sensors on the rig and recorded to the POROS 2 software in real

234 time. Displacement was applied to the inline grip 1 at a rate of 5 µm/sec and paused at every

235 0.2 mm travel. While paused, imaging and texture data were measured. To measure micro-

236 strains, SEM scans were performed using secondary electrons (SE2) with 20 keV voltage.

237 These images were then post-processed with LaVision's DIC software (DaVis 10) [32].

238 Using a subset size of 25 µm and step size of 8 µm, the software tracked the motion of

239 microstructural features on the samples during the test to produce contour plots of strains that

240 showed the evolution of microstructural strains. This procedure of strain measurement was

241 previously developed and demonstrated in our experimental facility [19,33]. This method is

242 capable of a displacement accuracy of 0.01 pixels with a strain resolution of about 0.1%

243 [18,32]. We used the software manufacturer's recommended subset size of 25 µm and it

244 corresponded to 13 µm length resolution in AA5182-O and 8 µm length resolution in DP600

245 micrographs. This accuracy has been demonstrated to be sufficient for the purpose of

246 microstructural strain measurement [18].

247   Texture was measured with the SEM's EBSD detector. Samples were scanned with the

248 step size of 0.5 µm. The raw data from the EBSD was then post-processed in the HKL

249 Channel 5 software to evaluate the inverse pole figure (IPF) maps. The in-situ strain and

250   texture measurements allowed a demonstration of the capability of the experiment to relate

251   microstructural evolution during the continuous strain path change.

4   Results and discussion

253   FE predictions of strain path change were validated in aluminium and steel using

254   measurements of strain evolution at the macroscale using DIC (Section 4.1). Once validated,

255   the technique was used to demonstrate the ability of the technique to capture the micro-strain

256   (Section 4.2.1) and texture (Section 4.2.2) evolution of material microstructure. Linking

257   macro-strain and micro-strain evolution during the continuous strain path change provided an

258   understanding between the plastic deformation and microstructural strain evolution.

259   Thereafter, the correlation study would reveal how the strain development during continuous

260   strain path change effected the microstructural features.

4.1   Validation of the design of the experimental method with digital image correlation

262   The design of the sample and the rig was validated by measuring the macro-strain

263   evolution in the samples using digital image correlation and comparing it to the FE

264   predictions. Macro-strains were tracked in the x- (ε_x) and y-axes (ε_y). The predicted evolution

265   of ε_x and ε_y strains in the AA5182-O and DP600 specimens during the tests are shown in

266   Figure 4 and Figure 5 respectively.

13

267
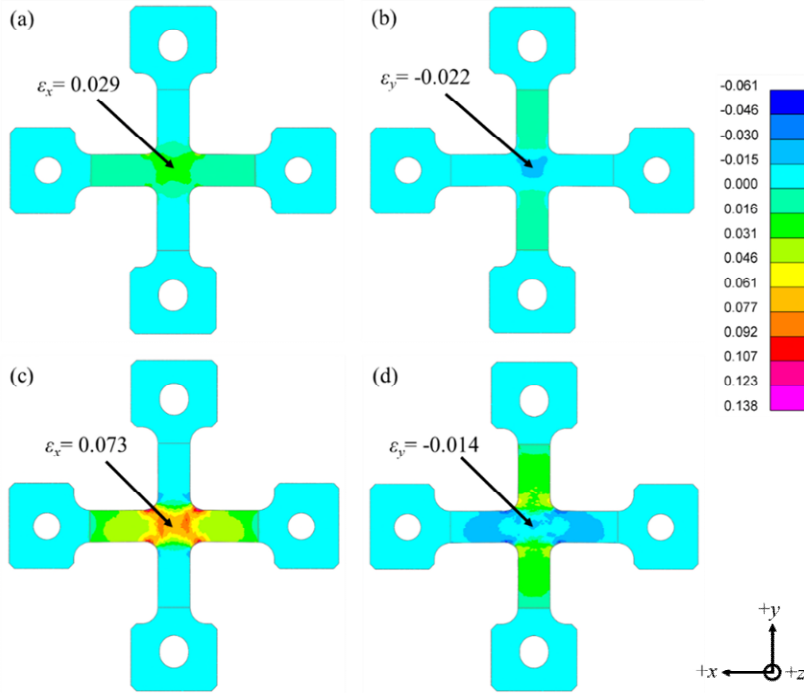
Figure 4: Predicted macro-strain in AA5182-O specimen during continuous strain path change: (a) ε_x and (b) ε_y strain distribution along uniaxial strain path before the strain path transition and (c) ε_x and (d) ε_y strain distribution after the strain path transition to biaxial strain path.

272
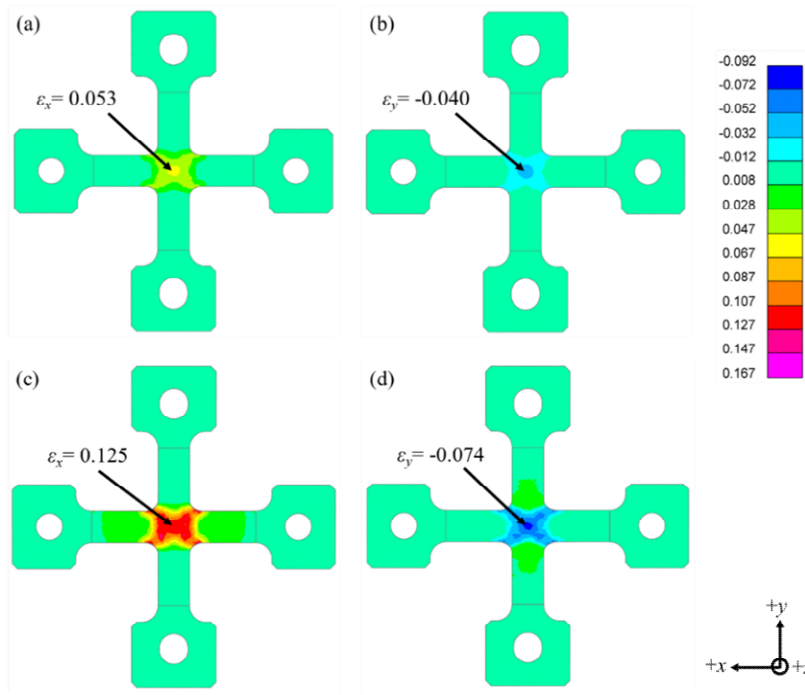
Figure 5: Predicted macro-strain in DP600 specimen during continuous strain path change:

(a) ε_x and (b) ε_y strain distribution along uniaxial strain path before the strain path transition

and (c) ε_x and (d) ε_y strain distribution after the strain path transition to biaxial strain path.

The corresponding experimental ε_x and ε_y strain contour of the AA5182-O and DP600

specimens before and after the strain path transition are presented in Figure 6a-d and Figure

7a-d respectively. The predictions of Figure 4 and Figure 5 and the experimental

measurements of Figure 6 and Figure 7 showed a similar pattern of strain distribution at the

central region. The behaviour of the evolving strain and its level of the simulated macro-

strain contours were reasonably similar (within 20% difference) between the predicted and
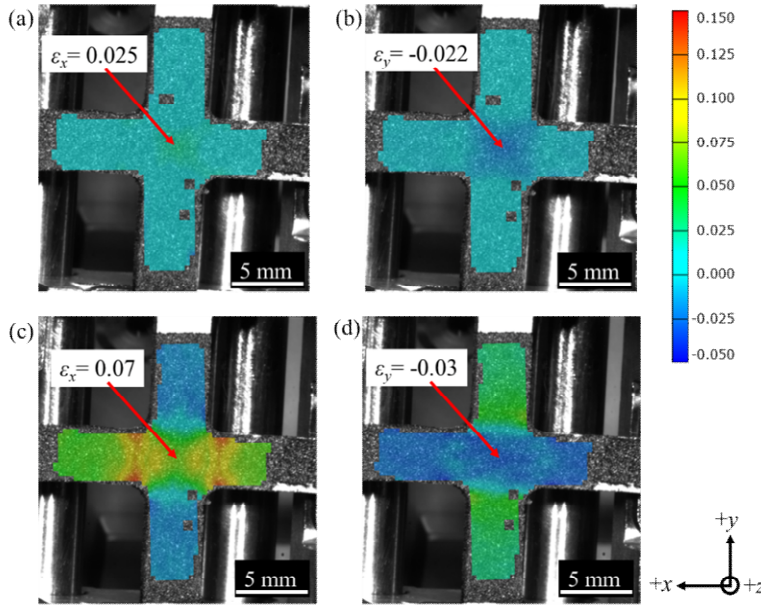
experimental strains.

15

283

Figure 6: Experimental macro-strain in AA5182-O specimen during continuous strain path change: (a) ε_x and (b) ε_y strain distribution along uniaxial strain path before the strain path transition and (c) ε_x and (d) ε_y strain distribution after the strain path transition to biaxial strain path.

288
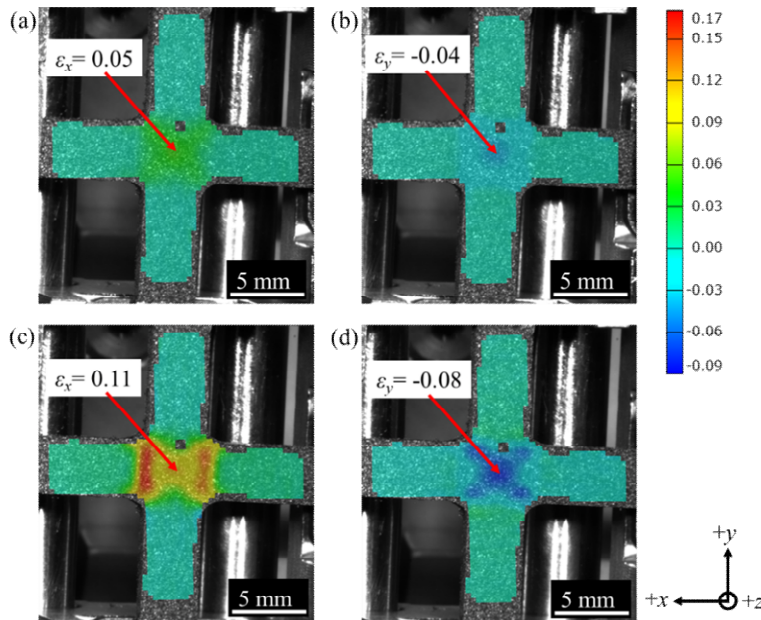
Figure 7: Experimental macro-strain in DP600 specimen during continuous strain path change: (a) ε_x and (b) ε_y strain distribution along uniaxial strain path before the strain path

291   transition and (c) ε_x and (d) ε_y strain distribution after the strain path transition to biaxial strain

292   path.

293   The measured evolution of average ε_x and ε_y strains at the central thinned regions in

294   both materials was compared to the respective predicted strain evolution in strain space

295   (Figure 8). The strain evolution confirmed that the continuous strain path change was

296   achieved during the experiments. It was shown from experimental strain path transition data

297   of aluminium and steel that the 0.2 mm slots served the purpose well and the continuous

298   transition was achieved with a reasonable amount of strain at biaxial strain path before

299   sample failure. Figure 8 shows that the continuous strain path change deformation was

300   divided into three stages. First, deformation occurred along the 'uniaxial' strain path. Second,

301   there was a period when deformation transitioned and lastly, deformation occurred along the

302   'biaxial' strain path. Figure 8 shows that the DP600 material deformed uniaxially until about

303   0.11 major strain ($\varepsilon_x = 0.11$) before transitioning to the biaxial strain path. For AA5182-O, the

304   transition was observed to occur at 0.04 major strain ($\varepsilon_x = 0.04$). The manner in which strain

305   developed during uniaxial elongation was different in both the materials because the 0.2 mm

306   slot length was fixed for the uniaxial extension of both materials. Differences in modulus,

307   plastic behaviour and anisotropy of aluminium and steel specimen affected the strain path of

308   the materials. In addition, as DP600 steel was thinner at the central region (0.25 mm for

309   DP600 and 0.3 mm for AA5182-O), higher levels of strain were induced during uniaxial

310   deformation in DP600 sample. This design allows the slot length and thickness of the central

311   region to be adjusted if a specific strain path is desired in future.

312   The slopes of the uniaxial strain path obtained from experiment was -0.75 for DP600

313   and -0.85 for AA5182-O, which was between uniaxial tension (slope = -0.5) and pure shear

314   deformation (slope = -1.0). The transition phase from uniaxial to biaxial strain paths (Figure

315   8) for AA5182-O and DP600 was visibly different. The transition for AA5182-O was smooth

316   and curved, indicating a gradual strain path transition while the transition curve for the

317   DP600 sample was sharp as from uniaxial strain path to biaxial strain path (Figure 8). This

318   difference in the transition curve was likely due to intrinsic material behaviour during the

319   continuous strain path transition because the applied loading was similar for both materials.

320   The measured slope obtained in biaxial strain path was +1.2 for DP600 and +0.35 for

321   AA5182-O. The slope of equibiaxial strain path is +1. This difference in slope was suspected

322   to be, in part, due to local deformation around the slots. Because AA5182-O and DP600 have

323   different modulus, plastic behaviour and anisotropic properties, this may have led to

324   differences in compliance in the sample. This may be addressed in future work by using

325   thicker samples of aluminium. The amount of strain induced during the biaxial path was less

326   in DP600 than AA5182-O before reaching the fracture strain values for both the materials as

327   the DP600 samples were already induced a higher amount of strain before starting the biaxial

328   stretching than AA5182-O samples.

329   The predicted and measured slopes were similar for both materials during uniaxial

330   loading. However, there were significant difference in the slope during the biaxial loading

331   phase because the predictions were based on a von Mises isotropic material model. Whereas

332   the anisotropy coefficient of the DP600 was nearly 1, the anisotropy coefficient for AA5182-

333   O was 0.8 (Table 1). As a result, the prediction of strain evolution for DP600 was better than

334   for AA5182-O. More advanced material models that account for anisotropic behaviour and

335   hardening were beyond the scope of the current research because the current aim was to

336   develop the technique rather than improve the prediction.

Experimental vs predicted strain evolution during continuous strain
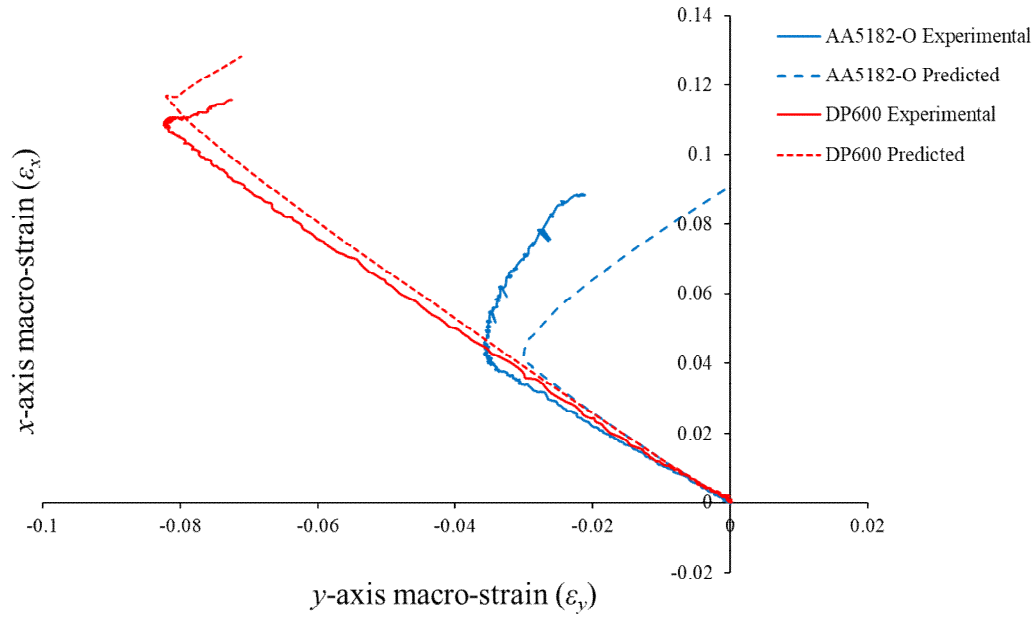path change in AA5182-O and DP600

Figure 8: Experimental vs predicted average strain evolution during continuous strain path
change at the central thinned region in AA5182-O and DP600 samples.

4.2 Strain and texture evolution in microstructure during continuous strain path change

To demonstrate the ability to measure the microstructural evolution of the sample
during a continuous strain path change, the rig was placed in an SEM to measure strain and
texture evolution. Separate tests were performed for strain and texture measurements. Texture
data was processed to track the changes in grain orientation. Each test was interrupted at
every 0.2 mm of extension to capture micrographs and texture images of the microstructure
for strain and texture measurements respectively. The interrupted locations are shown as
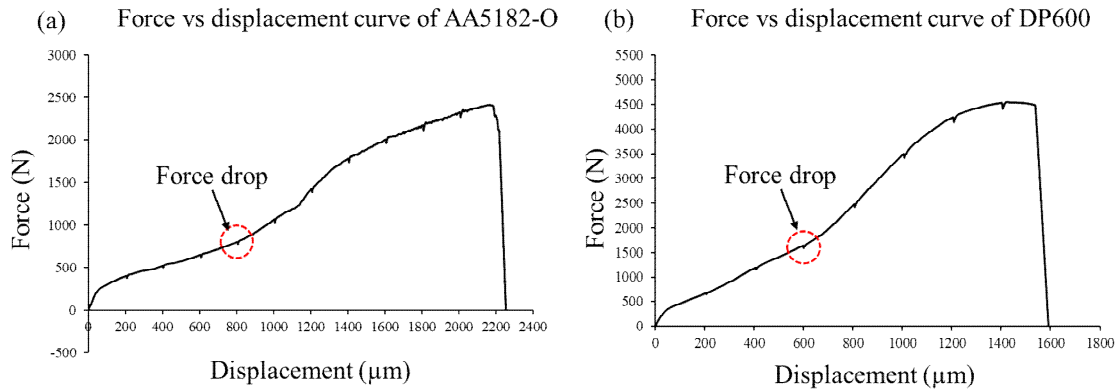drops in force in the force vs displacement curve (Figure 9).

19

Figure 9: Force vs displacement curve of (a) AA5182-O and (b) DP600 when elongation was interrupted at every 0.2 mm of extension with the interrupted locations shown as drops in force.

4.2.1 Microstructural strain evolution during strain path change

The micrographs (Figure 10 and Figure 11) of the sample surface obtained from SEM scans were analysed with DIC analysis to demonstrate the capability of the experiment to quantify microstructural strain (micro-strains) evolution along the x-axis (e_x). Figure 10 shows the result for AA5182-O and Figure 11 shows the results for DP600. The rectangular regions in Figure 10 and Figure 11 were tracked during the entire experiment and the strain distribution was calculated on this region using DIC analysis. The micro-strain contour plots are overlaid on the micrographs to show that the heterogeneous strain distributions in both materials (Figure 10 and Figure 11).

The spread of the heterogeneous strain distribution in the single phase AA5182-O was 0.2 to 0. The spread of strain in DP600 was 0.19 to 0.06. As DP600 steel is constituted of softer ferrite and harder martensite phase, strain localisation was mainly confined on softer ferrite phase. Similar findings were reported by Ghadbeigi et al. [18]. On the other hand, AA5182-O is constituted of a single phase matrix and a non-uniform strain field was developed on the microstructure where some grains were more strained than others. Similar

20

368   type of strain localisation was observed by Martin et al. [34] in a single phase magnesium

369   alloy. Further, Gao et al. [35] concluded that generally non-uniform strain field was induced

370   at the grain scale due to dislocation movement during plastic deformation.

371   The transition in loading can be seen in the way the pattern of the contour plots

372   evolved during the tests. A banding angle of e_x strains (indicated by black line in Figure 10

373   and Figure 11) rotated from approximately 50° to 52° for AA5182-O and approximately 45°

374   to 62° for DP600. The largest rotation taking place after the strain path transition, particularly

375   for DP600 (Figure 11). Before the strain path change, the banding angles were only rotated 1°

376   for both the materials. However, following the strain path transition, the angles were rotated

377   by 1° for AA5182-O and 16° for DP600. The unique ability to investigate behaviour of

378   AA5182-O and DP600 under transitioning loading will provide fresh understanding of the

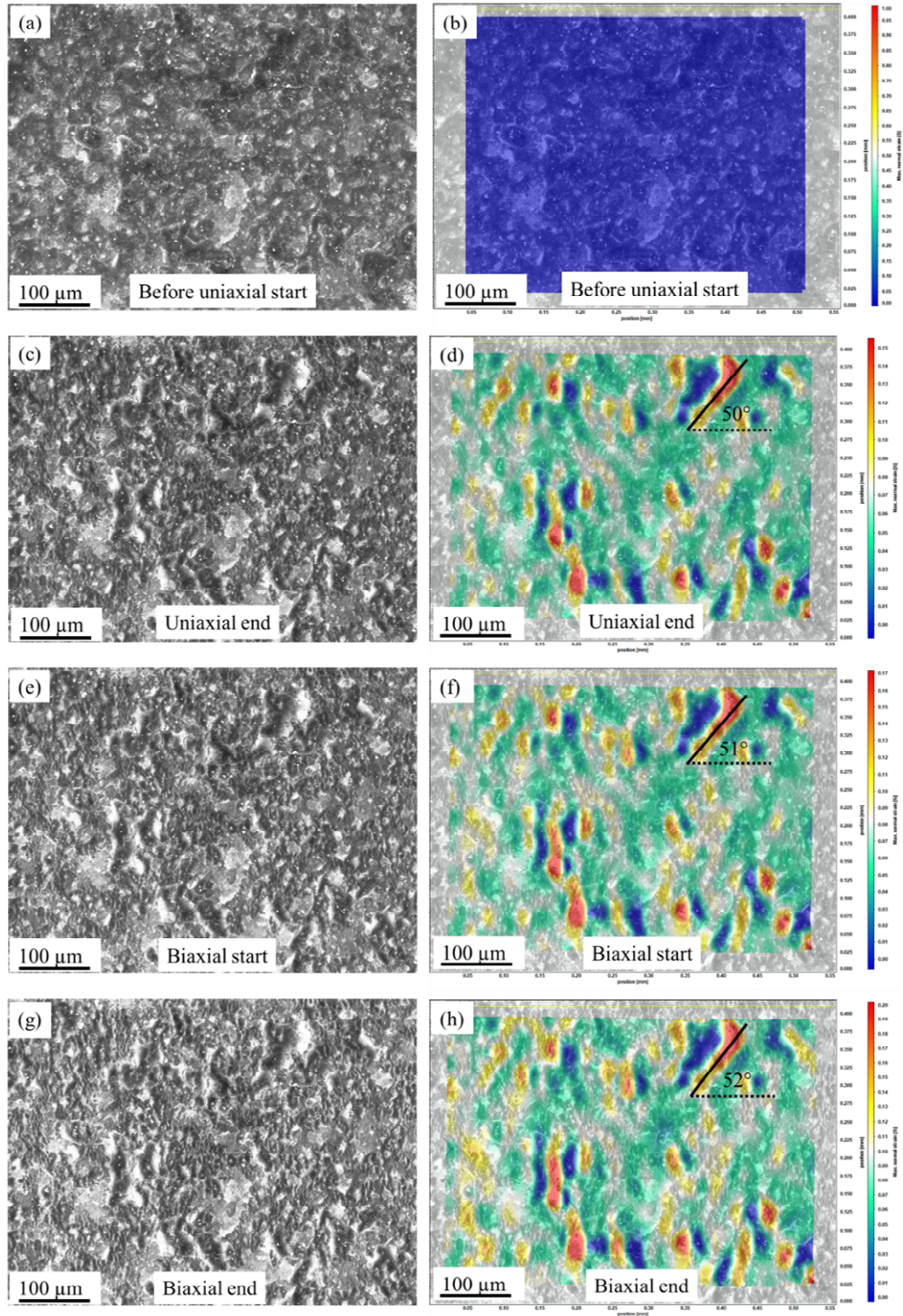379   intrinsic material behaviour of AA5182-O and DP600.

380

381

Figure 10: Micrographs of the centre of the AA5182-O specimen at (a) before uniaxial start, (c) uniaxial end, (e) biaxial start and (g) biaxial end during the strain path transition. Corresponding *x*-axis micro-strain (e_x) distribution calculated from micro DIC analysis at (b) before uniaxial start, (d) uniaxial end, (f) biaxial start and (h) biaxial end during the strain path transition.
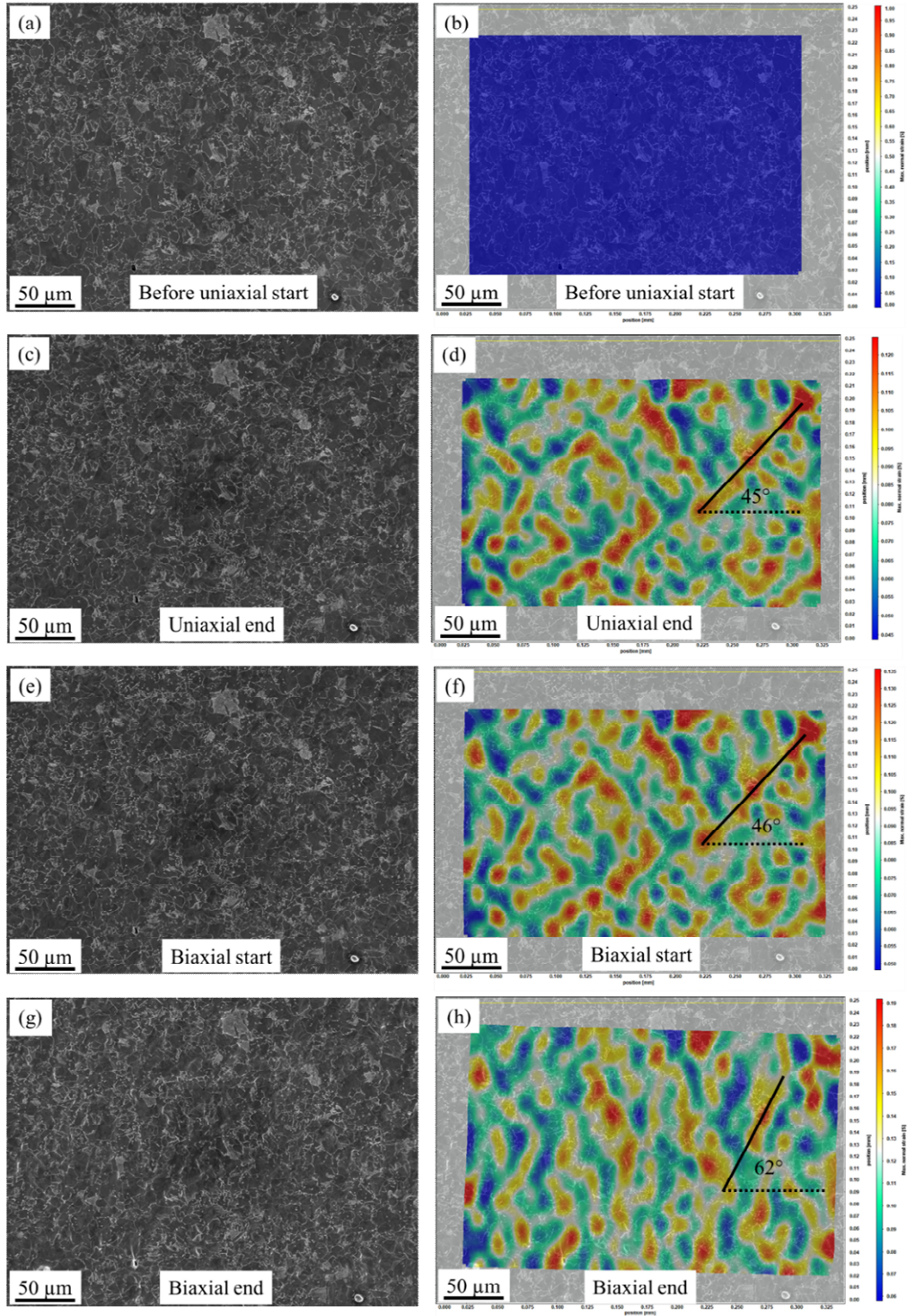
22

Figure 11: Micrographs of the centre of the DP600 specimen at (a) before uniaxial start, (c) uniaxial end, (e) biaxial start and (g) biaxial end during the strain path transition. Corresponding x-axis micro-strain (e_x) distribution calculated from micro DIC analysis at (b) before uniaxial start, (d) uniaxial end, (f) biaxial start and (h) biaxial end during the strain path transition.

4.2.2 Microstructural texture evolution during continuous strain path change

393

394   The rig was able to highlight and provide insight into the evolution of microstructural

395   texture during the continuous strain path change. Texture analysis was performed using the

396   EBSD detector in the SEM to map around 160 grains and 300 grains in the central thinned

397   regions of the AA5182-O and DP600 samples respectively. The EBSD (along X direction)

398   maps, SEM images and inverse pole figure (IPF) X maps of AA5182-O and DP600 samples

399   are shown in Figure 12 and Figure 13 respectively. Evidence of deformation was visually

400   clear within the grain structure of both materials, with grain elongation and shape change

401   occurring with increased elongation of both the samples. The microstructure showed a clear

402   change in texture from the end of uniaxial loading to biaxial loading. The EBSD and IPF

403   maps in Figure 12 and Figure 13 demonstrate, for the first time, textural changes of AA5182-

404   O and DP600 materials respectively during a continuous strain path change.

405   The EBSD images of AA5182-O showed that the uniaxial strain path caused rotation

406   of grains oriented in [101] crystallographic direction towards [001] direction (highlighted by

407   black dotted circles in Figure 12). In the next biaxal stage, the orientation of those grains

408   remained nearly same as [001]. However, in the biaxial phase, grains oriented in [101]

409   direction rotated towards [111] direction (highlighted by black circles in Figure 12). In the

410   first uniaxial stage, the orientation of those grains remained as more or less [101]. Hence, the

411   experiment was able to show that the strain path transition triggered a mechanism, which

412   compelled some grains to rotate while it hindered rotation of other grains. The increase in

413   plastic deformation at the sample surface was shown by the increase in slip bands in SEM

414   images captured during the deformation process (Figure 12). IPF X maps (Figure 12) showed

415   the gradual increase of multiples of uniform distribution (MUD) value of [111] and [001]

416   grains with a maximum intensity factor of around 2 and 2.64 respectively while MUD value

417   of [101] remained same as 1 at the end of the uniaxial strain path. During strain path

418   transition, the MUD value of [111] and [001] grains increased to 2.73 while the MUD value

419   of [101] grains diminished from 1 to nearly 0.04. During the biaxial strain path, the MUD

420   value of [111] and [001] grains increased to 3.16 whereas the MUD value of [101] grains

421   further reduced to 0.03. Hence, strain path transition triggered the increase of MUD value of

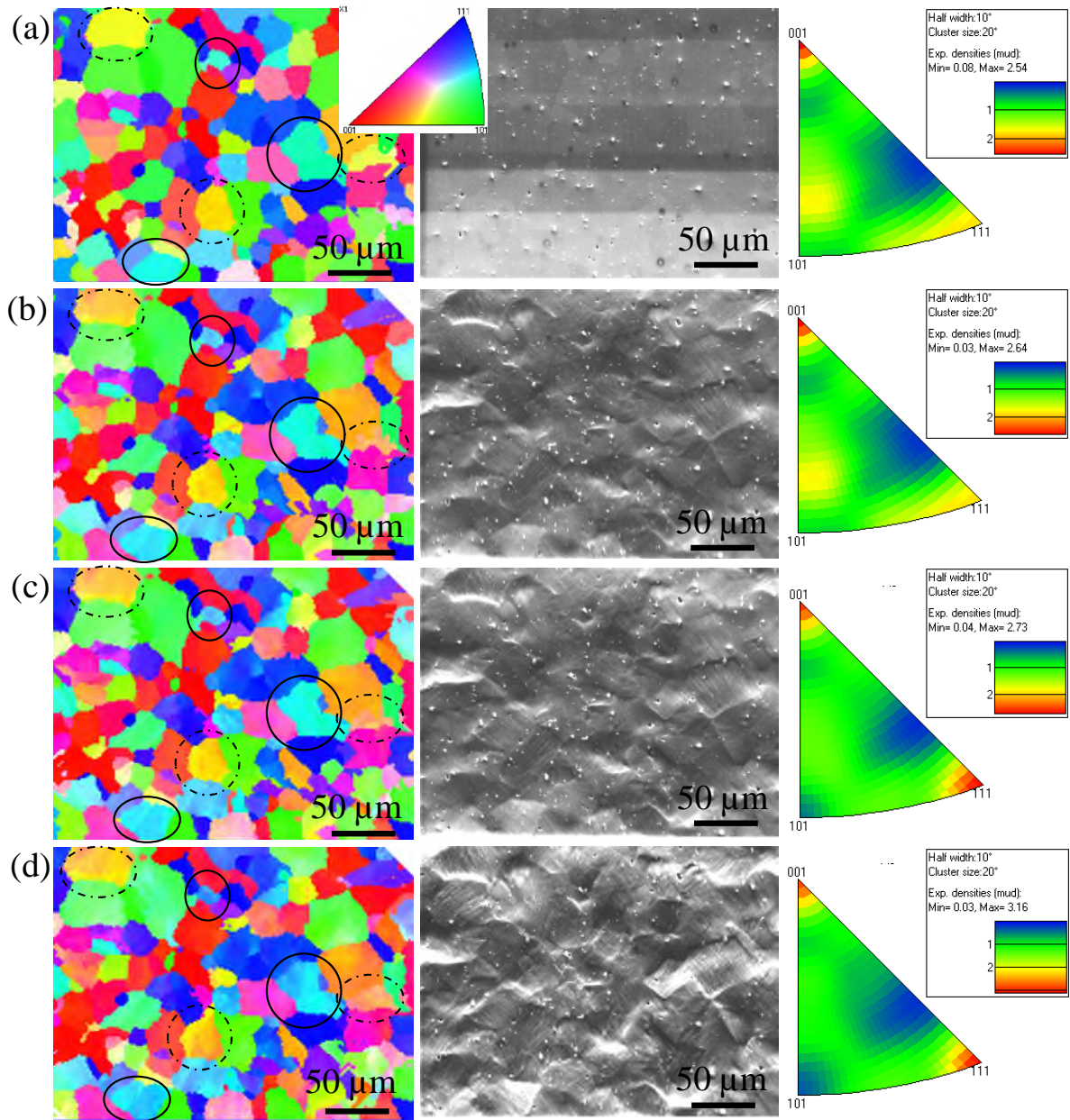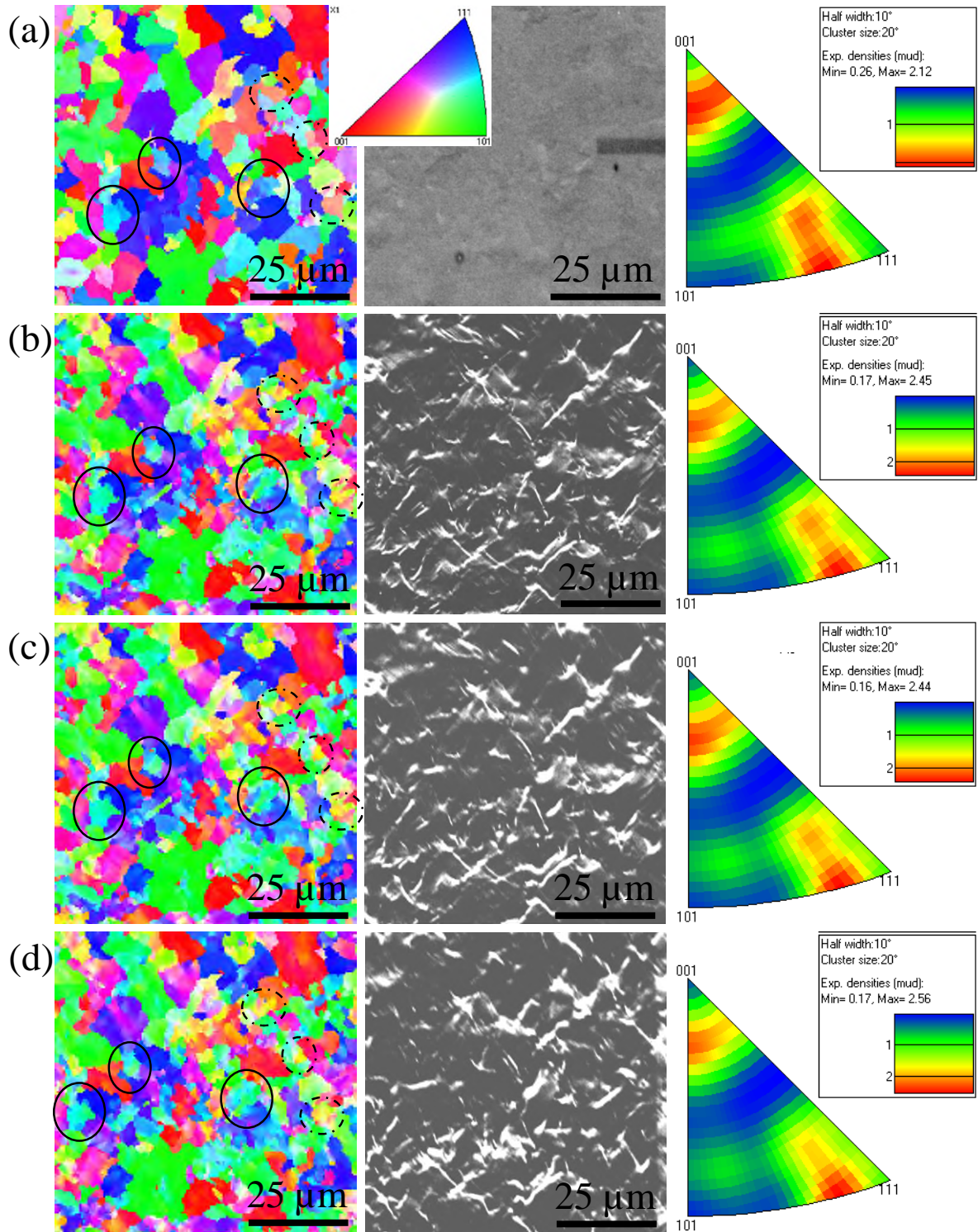422   [111] and [001] grains and reduction of MUD value of [101] grains.

Figure 12: On the left: EBSD mappings, in the middle: SEM images and on the right: inverse pole figure (IPF) X mapping of the centre of the AA5182-O specimen at (a) uniaxial start, (b) uniaxial end, (c) biaxial start and (d) biaxial end during continuous strain path change.

Similarly, EBSD images of DP600 showed [001] grains (highlighted by black dotted circles in Figure 13) and [111] grains (highlighted by black circles in Figure 13) rotated towards [101] direction in the uniaxial phase of the experiment. However, no rotations were observed during the transition to the biaxial strain path. Hence, the strain path transition

26

431   triggered a mechanism, which hindered rotation of some grains that rotated in the uniaxial

432   deformation stage and maintained the orientation of the grains same during the following

433   biaxial deformation stage. The plastic deformation of the sample surface increased

434   dislocation densities and it was prominent from the increase in slip bands in SEM images

435   captured during the deformation process (Figure 13). IPF X maps (Figure 13) showed the

436   decrease of multiples of uniform distribution (MUD) value of [001] grains from 1 to nearly

437   0.17 and the MUD values of [101] and [111] grains remained nearly constant at 0.17 and 1

438   respectively during uniaxial strain path. In subsequent stages of strain path transition and

439   biaxial strain path, the MUD values of [001], [101] and [111] grains were remained same.

440   Hence, strain path transition kept the MUD value of the grains unchanged while the MUD

441   values of those grains changed in the initial uniaxial deformation stage.

442

443

Figure 13: On the left: EBSD mappings, in the middle: SEM images and on the right: inverse

pole figure (IPF) X mapping of the centre of the DP600 specimen at (a) uniaxial start, (b)

uniaxial end, (c) biaxial start and (d) biaxial end during continuous strain path change.

447   This novel mechanism was able to reveal, for the first time, how a strain path transition

448   affects the rotation of grains. In the two materials studied here, the strain path change

449   promoted the rotation of some grains while it hindered the rotation of other grains depending

450   on the crystallographic orientation of the grains. In future, a detailed comparison on grain

451   rotation with the help of microstructure and texture evolution in between continuous and

452   discontinuous strain path change may give some insights regarding how the grains are

453   rotating during the continuous strain path transitions that take place in the draw stage of a

454   stamping process. In addition, tracking of other microstructural features namely Taylor

455   factor, geometric necessary dislocation (GND) density and local misorientation may reveal

456   the microstructural evolution in more details during continuous strain path change.

457 5   Conclusions

458   An experimental technique was developed to deform cruciform samples initially along a

459   uniaxial strain path and then along a biaxial strain path continuously without unloading the

460   sample. This was achieved with a unique sample design. The experimental technique utilised

461   a simple biaxial stretching rig and a simple sample geometry to perform continuous strain

462   path change. DIC analysis was performed on steel and aluminium samples and showed that

463   the technique was able to change the strain path in both materials continuously without

464   unloading the sample. Therefore, the novelty of the developed testing method is to achieve

465   strain path change continuously without removing applied load from the sample in a biaxial

466   stretching mechanism by providing slotted holes in two arms out of four arms of a cruciform

467   test specimen. By changing the slot length, the point of strain path transition can be changed

468   accordingly. As the overall set-up can be placed inside an SEM chamber, in-situ analyses can

469   be carried out to identify microstructural changes to the material during the continuous strain

470   path change. In particular, SEM images and EBSD data were captured in-situ during the

471 deformation process. The SEM images were post processed to study strain evolution in the

472 microstructure while the EBSD data revealed the changes of texture during the deformation

473 process. Based on the results obtained from this study, the following conclusions were drawn:

474 - The experimental method was able to change the strain path from uniaxial to the biaxial
475   strain path in steel and aluminium continuously, without unloading the sample.

476 - The strain path change curve obtained from the experiments correlated well with the
477   predicted curve from the FE model of the mechanism.

478 - The experimental method allowed observation into the differences in the manner in
479   which the strain path change occurs in aluminium and steel. The strain path transition
480   for AA5182-O was a gradual transition from uniaxial to biaxial strain. On the other
481   hand, the transition in the DP600 sample was sharp and rapid from uniaxial to biaxial
482   strain.

483 - The evolution of material microstructure can be observed because the loading rig can
484   be mounted in a SEM. Initial observations showed a rotation in micro-strain banding
485   angle in both the materials. The rotation was higher in DP600 sample.

486 - The textural data captured during the strain path change revealed that the strain path
487   change triggered a mechanism, which either promoted or hindered the rotation of the
488   grains depending on their crystallographic orientations.

Credit Author Statement

Sisir Dhara: Conceptualization; Microstructural/ mechanical analysis; Investigation; Methodology; Interpretation of data; Writing - original draft.

Scott Taylor: Interpretation of data; Experimentation; Project administration; Supervision; Writing review & editing.

Lukasz Figiel: Supervision; Writing review & editing.

Darren Hughes: Supervision; Writing review & editing.

Sumit Hazra: Interpretation of data; Experimentation; Funding acquisition; Project administration; Supervision; Writing review & editing.

Data availability

The raw/processed data required to reproduce these findings cannot be shared at this time as the data also forms part of an ongoing study.

References

[1] Dhara S, Basak S, Panda SK, Hazra S, Shollock B, Dashwood R. Formability analysis of pre-strained AA5754-O sheet metal using Yld96 plasticity theory: Role of amount and direction of uni-axial pre-strain. J Manuf Process 2016;24:270–82. https://doi.org/https://doi.org/10.1016/j.jmapro.2016.09.014.

[2] Collins DM, Erinosho T, Dunne FPE, Todd RI, Connolley T, Mostafavi M, et al. A synchrotron X-ray diffraction study of non-proportional strain-path effects. Acta Mater 2017;124:290–304. https://doi.org/https://doi.org/10.1016/j.actamat.2016.11.011.

[3] Song X, Leotoing L, Guines D, Ragneau E. Effect of continuous strain path changes on forming limit strains of DP600. Strain 2019;55:e12329. https://doi.org/https://doi.org/10.1111/str.12329.

[4] Leotoing L, Guines D. Investigations of the effect of strain path changes on forming

limit curves using an in-plane biaxial tensile test. Int J Mech Sci 2015;99:21–8.

https://doi.org/https://doi.org/10.1016/j.ijmecsci.2015.05.007.

[5]   Stoughton TB. A general forming limit criterion for sheet metal forming. Int J Mech

Sci 2000;42:1–27. https://doi.org/https://doi.org/10.1016/S0020-7403(98)00113-1.

[6]   Stoughton TB, Zhu X. Review of theoretical models of the strain-based FLD and their

relevance to the stress-based FLD. Int J Plast 2004;20:1463–86.

https://doi.org/https://doi.org/10.1016/j.ijplas.2003.11.004.

[7]   Yoshida K, Kuwabara T, Kuroda M. Path-dependence of the forming limit stresses in a

sheet metal. Int J Plast 2007;23:361–84.

https://doi.org/https://doi.org/10.1016/j.ijplas.2006.05.005.

[8]   Yoshida K, Kuwabara T. Effect of strain hardening behavior on forming limit stresses

of steel tube subjected to nonproportional loading paths. Int J Plast 2007;23:1260–84.

https://doi.org/https://doi.org/10.1016/j.ijplas.2006.11.008.

[9]   Verma RK, Kuwabara T, Chung K, Haldar A. Experimental evaluation and

constitutive modeling of non-proportional deformation for asymmetric steels. Int J

Plast 2011;27:82–101. https://doi.org/https://doi.org/10.1016/j.ijplas.2010.04.002.

[10]   Erinosho TO, Cocks ACF, Dunne FPE. Coupled effects of texture, hardening and non-

proportionality of strain on ductility in ferritic steel. Comput Mater Sci 2013;80:113–

22. https://doi.org/https://doi.org/10.1016/j.commatsci.2013.03.002.

[11]   Erinosho TO, Cocks ACF, Dunne FPE. Texture, hardening and non-proportionality of

strain in BCC polycrystal deformation. Int J Plast 2013;50:170–92.

https://doi.org/https://doi.org/10.1016/j.ijplas.2013.04.008.

[12]   Schlosser F, Signorelli J, Leonard M, Roatta A, Milesi M, Bozzolo N. Influence of the

541   strain path changes on the formability of a zinc sheet. J Mater Process Technol

542   2019;271:101–10. https://doi.org/https://doi.org/10.1016/j.jmatprotec.2019.03.026.

543   [13] Viatkina EM, Brekelmans WAM, Geers MGD. The role of plastic slip anisotropy in

544   the modelling of strain path change effects. J Mater Process Technol 2009;209:186–

545   93. https://doi.org/https://doi.org/10.1016/j.jmatprotec.2008.01.056.

546   [14] Zhang R, Xu Z, Peng L, Lai X, Fu MW. Modelling of ultra-thin steel sheet in two-

547   stage tensile deformation considering strain path change and grain size effect and

548   application in multi-stage microforming. Int J Mach Tools Manuf 2021;164:103713.

549   https://doi.org/https://doi.org/10.1016/j.ijmachtools.2021.103713.

550   [15] Thuillier S, Manach PY, Menezes LF. Occurence of strain path changes in a two-stage

551   deep drawing process. J Mater Process Technol 2010;210:226–32.

552   https://doi.org/https://doi.org/10.1016/j.jmatprotec.2009.09.004.

553   [16] Barata da Rocha A, Santos AD, Teixeira P, Butuc MC. Analysis of plastic flow

554   localization under strain paths changes and its coupling with finite element simulation

555   in sheet metal forming. J Mater Process Technol 2009;209:5097–109.

556   https://doi.org/https://doi.org/10.1016/j.jmatprotec.2009.02.008.

557   [17] Yang M, Dong X, Zhou R, Cao J. Crystal plasticity-based forming limit prediction for

558   FCC materials under non-proportional strain-path. Mater Sci Eng A 2010;527:6607–

559   13. https://doi.org/https://doi.org/10.1016/j.msea.2010.06.063.

560   [18] Ghadbeigi H, Pinna C, Celotto S, Yates JR. Local plastic strain evolution in a high

561   strength dual-phase steel. Mater Sci Eng A 2010;527:5026–32.

562   https://doi.org/https://doi.org/10.1016/j.msea.2010.04.052.

563   [19] Celotto S, Ghadbeigi H, Pinna C, Shollock BA, Efthymiadis P. Deformation-Induced

564   Microstructural Banding in TRIP Steels. Metall Mater Trans A 2018;49:2893–906.

565   https://doi.org/10.1007/s11661-018-4650-z.

566 [20] Caër C, Pesci R. Local behavior of an AISI 304 stainless steel submitted to in situ

567   biaxial loading in SEM. Mater Sci Eng A 2017;690:44–51.

568   https://doi.org/https://doi.org/10.1016/j.msea.2017.02.087.

569 [21] Bhargava M, Tewari A, Mishra S. Strain path diagram simulation of AA 5182

570   Aluminum alloy. Procedia Eng 2013;64:1252–8.

571   https://doi.org/https://doi.org/10.1016/j.proeng.2013.09.205.

572 [22] Wang K, Zhou B, Li J, Carsley JE, Li Y. Characterization of Plastic Anisotropy of

573   AA5182-O Sheets During Prestraining and Subsequent Annealing. J Manuf Sci Eng

574   2018;140. https://doi.org/10.1115/1.4040157.

575 [23] Chen ZT, Worswick MJ, Lloyd DJ. Damage-Based Finite Element Modeling of

576   Stretch Flange Forming of Aluminium-Magnesium Alloy. Mater. Sci. forum, vol. 519,

577   Trans Tech Publ; 2006, p. 815–20.

578 [24] Ju L, Patil S, Dykeman J, Altan T. Forming of Al 5182-O in a Servo Press at Room

579   and Elevated Temperatures. J Manuf Sci Eng 2015;137.

580   https://doi.org/10.1115/1.4030334.

581 [25] Basak S, Panda SK, Zhou YN. Formability Assessment of Prestrained Automotive

582   Grade Steel Sheets Using Stress Based and Polar Effective Plastic Strain-Forming

583   Limit Diagram. J Eng Mater Technol 2015;137:41006–12.

584 [26] Li J, Hu SJ, Carsley JE, Lee TM, Hector Jr. LG, Mishra S. Postanneal Mechanical

585   Properties of Prestrained AA5182-O Sheets. J Manuf Sci Eng 2011;133.

586   https://doi.org/10.1115/1.4004613.

587   [27]   Li J, Kim S, Lee TM, Krajewski PE, Wang H, Hu SJ. The effect of prestrain and

588   subsequent annealing on the mechanical behavior of AA5182-O. Mater Sci Eng A

589   2011;528:3905–14. https://doi.org/https://doi.org/10.1016/j.msea.2010.12.014.

590   [28]   Carvill J. Mechanical engineer's data handbook. Butterworth-Heinemann; 1994.

591   [29]   Farabi N, Chen DL, Li J, Zhou Y, Dong SJ. Microstructure and mechanical properties

592   of laser welded DP600 steel joints. Mater Sci Eng A 2010;527:1215–22.

593   https://doi.org/https://doi.org/10.1016/j.msea.2009.09.051.

594   [30]   Sutton MA, Orteu JJ, Schreier H. Image correlation for shape, motion and deformation

595   measurements: basic concepts, theory and applications. Springer Science & Business

596   Media; 2009.

597   [31]   GOM, GOM ARAMIS. 2009. https://www.gom.com/metrology-systems/aramis

598   (Accessed 27-03-2020).

599   [32]   LaVision, DaVis Strain Master Software, DaVis 10. 2017.

600   https://www.lavision.de/en/products/davis-software/ (Accessed 26-09-2021).

601   [33]   Alharbi K, Ghadbeigi H, Efthymiadis P, Zanganeh M, Celotto S, Dashwood R, et al.

602   Damage in dual phase steel DP1000 investigated using digital image correlation and

603   microstructure simulation. Model Simul Mater Sci Eng 2015;23:85005.

604   https://doi.org/10.1088/0965-0393/23/8/085005.

605   [34]   Martin G, Sinclair CW, Lebensohn RA. Microscale plastic strain heterogeneity in slip

606   dominated deformation of magnesium alloy containing rare earth. Mater Sci Eng A

607   2014;603:37–51. https://doi.org/https://doi.org/10.1016/j.msea.2014.01.102.

608   [35]   Gao H, Huang Y. Geometrically necessary dislocation and size-dependent plasticity.

609   Scr Mater 2003;48:113–8. https://doi.org/https://doi.org/10.1016/S1359-

610   6462(02)00329-9.

611